

# Microstructure Evolution and Mechanical Behaviour of SAW Weldments of CSEF Steel on Preheating and PWHT

Saurav Suman<sup>1,2</sup> · Pankaj Biswas<sup>1</sup> · Avinish Tiwari<sup>1</sup>

Received: 19 December 2019 / Accepted: 23 March 2020 / Published online: 16 April 2020  
© The Indian Institute of Metals - IIM 2020

**Abstract** In this study, double-sided submerged-arc-welded CSEF steel joints were considered for microstructural and mechanical (hardness, ductility and strength) characterisations for four different cases of preheating and PWHT processes. The XRD and EDS analyses were also performed to investigate the phase transformation and chemical composition. Preheating was observed to be an improving factor for ductility and hardness of the welds. Similarly, PWHT enhanced the uniformity in the hardness distribution owing to reduced austenitic grain size in the HAZ as well as equiaxed fine-grained ferrite matrix in the FZ. It was observed that preheating and combined preheating and PWHT increased the ductility of the weld by 16.9% and 56.3%, respectively, from the as-welded case. Furthermore, it was also observed that preheating individually and preheating combined with PWHT reduced the maximum hardness values by 8.2% and 60.2%, respectively.

**Keywords** SAW · CSEF steel · Preheating · PWHT

## 1 Introduction

Grade 91 steel is known for its creep strength at elevated temperature, good thermal conductivity and comparatively lower thermal expansion coefficient. So, it is also known as creep strength-enhanced ferrite steel. The steels with chromium percentage (9–12%) are preferable for

components in power plant like super-heater coils, headers, steam pipes, boilers, energy shells, etc. [1]. These steels also exhibit the good resistance against steam corrosion and hardenability due to the presence of Cr and small quantities of Ni and Mg [1]. The production of Grade 91 steel (9Cr–1Mo–NbV steel) involves the quenching and austenitising processes which introduce dislocation contents in its lath structure. It forms the precipitates of nitrides and carbides (MX types and  $M_{23}C_6$ ). Such precipitation strengthening processes increase the creep strength [2]. The heat treatment develops tempered martensite forming  $Cr_{23}C_6$  particles.  $Cr_xC_y$  (chromium carbide) in the tempered P91 steel provides its thermal stability due to relatively high copiousness of chromium in the matrix [3]. Still, it requires both preheating and post-welding heat treatment for better weld quality and desired mechanical properties. Preheating not only reduces the thermal gradient but also removes the possibilities of hydrogen-induced embrittlement in P91 steel welds, while post-weld heat treatment (PWHT) works as regaining process for complete martensitic structure in the weld. It recovers the mechanical properties like creep strength, room temperature hardness, toughness, etc. One of the most important factors in welding of P91 steel weld is type IV cracking failure [4]. Therefore, it is very important to specify the maximum suitable temperature up to which preheating and PWHT should be performed. For preheating, the maximum temperature depends on various factors such as chemical composition of the base metal, hydrogen diffusion, heat input and size of the weld component [5, 6]. To reduce hardness in weld HAZ and to gain the requisite toughness in weld deposits of high-resisting tempering material (i.e. Grade 91), higher PWHT temperature is required [3, 7–9].

✉ Saurav Suman  
sauravnitmz@gmail.com

<sup>1</sup> Indian Institute of Technology Guwahati, Guwahati, India

<sup>2</sup> National Institute of Technology Mizoram, Aizawl, India

Some of the most suitable welding processes for P91 steel are SMAW, EBW SAW, TIG/MIG and GTAW, etc. Among all, SAW or submerged arc welding process produces high current density, high welding speed, high metal deposition rate and good depth of penetration [10]. Various studies related to microstructural stability and its effects on mechanical properties of P91 steel weld are there for different arc welding processes. In spite of additional advantages of SAW process, very few studies are found on submerged arc-welded P91 steel welds till date. Santella et al. [11] conducted SAW process on P91 steel thick pipe to study the martensitic transformation and the changes in its creep behaviour along with that transformation. Zhang et al. [12] investigated the mechanical behaviour of the SAW-welded P91 steel for the effect of its precipitates. Roy et al. [13] performed the submerged arc welding with an additional amount of boron trioxide in the flux on P91 steel plate and investigated its effect on the microstructural and mechanical strengths of the weldments. For the first time, Rao and Kalyankar [14] conducted parametric study of SAW process on P91 steel to show their effects on weld bead shape and geometry, YS, UTS, hardness, etc.. Authors recently have performed some studies on the effect of SAW high heat input on P91 steel weld for residual stresses and deformations [15–19]. Therefore, submerged arc welding process with its great depth of penetration and current density can be the most suitable arc welding process for such a refractory steel, i.e. P91 steel plate of higher thickness with comparatively lesser number of passes. Hence, microstructural and thermo-mechanical investigations on SAW-welded P91 steel are also important. The comparative studies on the effects of preheating, PWHT and combined preheating and PWHT on SAW-welded P91 steel are also rarely found.

In this study, a double-sided double pass submerged arc welding of one of the CSEF steels, i.e. P91 steel, was considered. Preheating was performed before the actual welding process followed by post-weld heat treatment. In this way, four samples were developed for four different cases. To conduct mechanical and microstructural studies, different samples were prepared for microstructure optical imaging, hardness and tensile tests, etc., separately. It was observed that preheating could not only reduce the possibility of hydrogen embrittlement but also improved the mechanical properties in terms of higher ductility and smooth hardness distribution across the weld. On the other hand, PWHT recrystallised the grains particularly in HAZ and FZ, which resulted in fine equiaxed ferritic grains in FZ with cementite precipitates, while it refined the austenitic grain boundaries in HAZ. This phenomenon is termed as tempering. Such microstructural fruition diminished the mechanical strength of the weld, whereas the presence of different creep strength-enhancing elements and

precipitates was also observed after PWHT of the weld which was examined based on XRD and EDS results. Finally, it was observed that both preheating and PWHT weakened the YS and UTS of the weld on account of increase in fractional area of carbide precipitates.

## 2 Experimental Setup and Methodology

### 2.1 Material and Weld Preparation

ASME/ASTM SA/A 387 Grade 91 class 2 steel was selected with the thickness of 10 mm. Each sample was of dimensions  $150 \times 75 \times 10 \text{ mm}^3$ . The plate had been normalised at  $1050 \text{ }^\circ\text{C}$  with holding time of 1 min/mm and cooled in still air and then tempered at  $780 \text{ }^\circ\text{C}$  with holding time of 30 min followed by cooling in still air. A copper-coated low-alloyed welding wire (Make: ESAB, coded as OK AUTROD 13.20) of diameter 3.1 mm was selected as per the thickness of the plate and the diameter of the welding machine nozzle. Table 1 presents the chemical compositions of both P91 steel plate and the corresponding electrode wire. An agglomerated basic flux (Make: ESAB, coded as OK FLUX 10.62) recommended for the CSEF group of steels was used in the welding. Finally, a double-sided square butt weld joint welding was performed on the plate placed at the root gap of 2.5 mm gap. The welding was accomplished for four different cases with preheating, PWHT and combined preheating and PWHT as given in Table 2. A suitable set of welding parameters were obtained as given in Table 3. The complete setup of welding process is shown in Fig. 1.

### 2.2 Preheating and PWHT

The preheating temperature for P91 steel can be calculated from the relation given in Eq. (1) [5, 7, 20]. The preheating temperature was obtained in the range of  $250\text{--}300 \text{ }^\circ\text{C}$  based on the chemical configuration of weld plate, hydrogen diffusion and amount of heat supplied [6]. A preheating temperature of maximum  $300 \text{ }^\circ\text{C}$  was maintained and controlled with the help of thermocouple and infrared thermal imaging.

$$T_p = 697 \times \text{CET} + 160 \times \tanh\left(\frac{t}{35}\right) + 62 \times \text{HD}^{35} + (53 \times \text{CET} - 32) \times Q - 328 \quad (1)$$

where  $T_p$ , preheat temperature ( $^\circ\text{C}$ ); CET, carbon equivalent;  $t$ , thickness of the plate (mm); HD, hydrogen diffusion and  $Q$ , input (kW) [13]. Post-welding heat treatment was performed in an automatic furnace within 48 h after the actual welding process. AWS suggested that heating at  $730 \text{ }^\circ\text{C}$  for 1 h is the minimum required

**Table 1** Chemical configuration of ASTM A387 Gr. 91 steel and electrode wire (wt%)

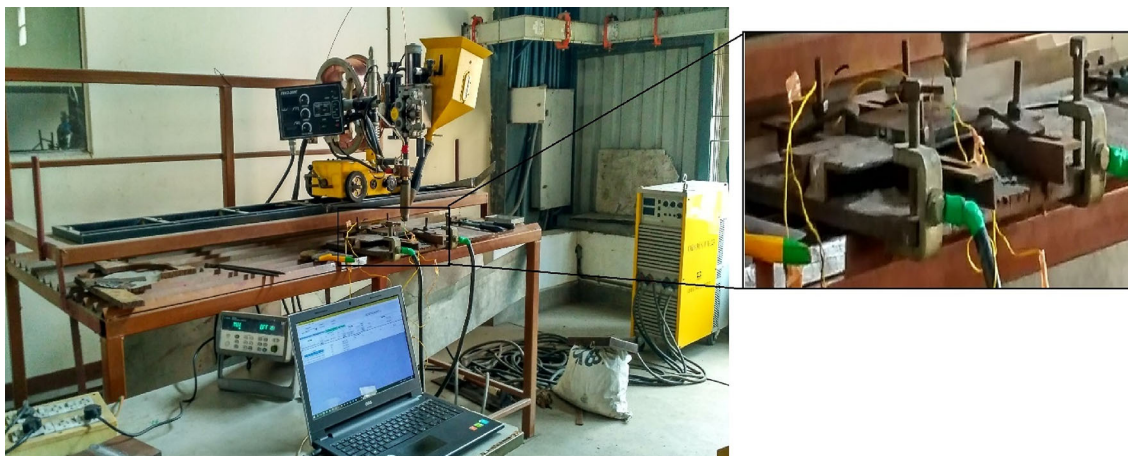
Elements	C	Si	Mn	P	S	Cr	Mo	V	B	N	Ni
P91 steel plate	0.1	0.29	0.46	0.016	0.001	8.69	0.89	0.22	0.001	0.039	0.27
Electrode wire	0.11	0.16	0.7	0.008	0.002	4.28	0.9	0.01	0.07	0.0067	0.05

**Table 2** List of samples with different cases

Processes performed	As-welded	Preheated	PWHT	Preheated and PWHT
Preheating	✗	✓	✓	✗
PWHT	✗	✓	✗	✓

**Table 3** Process parameters for each pass of double-sided SAW experiment

Process parameters	Current (A)	Voltage (V)	Travel speed (mm/s)	Length of stick out (mm)
Value	470	22.5	5.1	25

**Fig. 1** Set-up of submerged arc welding process

temperature for PWHT [14, 15]. Taking the appropriate weld toughness into consideration, a parameter termed as ‘*P*’ (Larson–Miller parameter) was defined which determined the required PWHT temperature. The parameter ‘*P*’ is shown as in Eq. (2) [21, 22].

$$P = k(\log t + C) \times 10^3 \quad (2)$$

where *C*, material-specific constant; *k*, soak temperature (Kelvin) and *t*, holding time (h). If the value taken for *C* was 21, the minimum PWHT temperature was obtained as 760 °C with holding time of 2 h [8, 23]. Hence, the heating was carried out at a rate of 100–150 °C till the temperature below the recrystallisation temperature, i.e.

760 °C. Then, for annealing, the sample was held for 2 h at 760 °C. Cooling was performed finally at the rate of 150 °C followed by cooling in the air to regain the martensitic structure in the weld zone [6].

### 2.3 Metallographic Examination

The cross-sectional images were captured for all the weld samples using a macroscopic digital camera (Make: Nikon) to examine the overall weld quality. Microstructure characterisation was performed across the weldment for different zones on an optical microscope (Make: Carl Zeiss). To reveal the microstructure, samples were polished with

emery paper with grades varying from coarse to fine size. Finally, the exposed surface was etched in the solution of Vilella's reagent (100 ml ethanol + 2–3 g picric acid + 4–5 ml hydrochloric acid) [24]. Micrograph was obtained for different zones, i.e. base metal zone, weld fusion zone and heat-affected zone (HAZ). HAZ itself was categorised as coarse grain (CG) HAZ and fine grain (FG) HAZ along with intercritical HAZ.

## 2.4 Hardness and Tensile Tests

The hardness measurement was taken on a Vickers hardness tester (Make: Omni Tech) on the marked points along

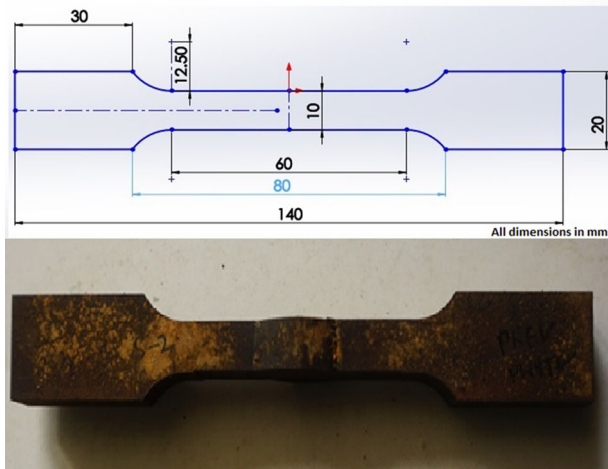


**Fig. 2** Tensile sample and its dimensions

a line across the weld. The dwelling load of 2 kg was gradually applied with 10 s of dwelling time. Two lines were marked separately for both sides of weldments passing through the top and bottom extreme portions of the weld bead as shown in Fig. 3. The influence of preheating and PWHT on UTS, YS and ductility of the welds was specified by conducting tensile test. ASTM E8-04 standard flat specimens were prepared without removing the weld bead shown in Fig. 2. The gauge length was 60 mm. A strain rate of 0.1 mm/s was decided to conduct the tensile test in the room temperature environment. It was also conducted for the base metal to compare the results. All the tests were performed on a universal hydraulic servo-controlled machine (250 kN, Make: BISS MODEL, MEDIAN 250).

## 2.5 XRD, FESEM and EDS Analyses

For phase change determination, the intensity variation at different angles was recorded through an X-ray diffractometer (Make: Rigaku). Scanning electron micrograph (SEM) analysis was also conducted for fractography of tensile fractured samples to investigate the nature of the fracture surface. The chemical composition was characterised for quantitative analysis of different elements in the weld before and after the PWHT along with the composition in base metal with the help of energy-dispersive (X-ray) spectroscopy also known as EDS analysis.

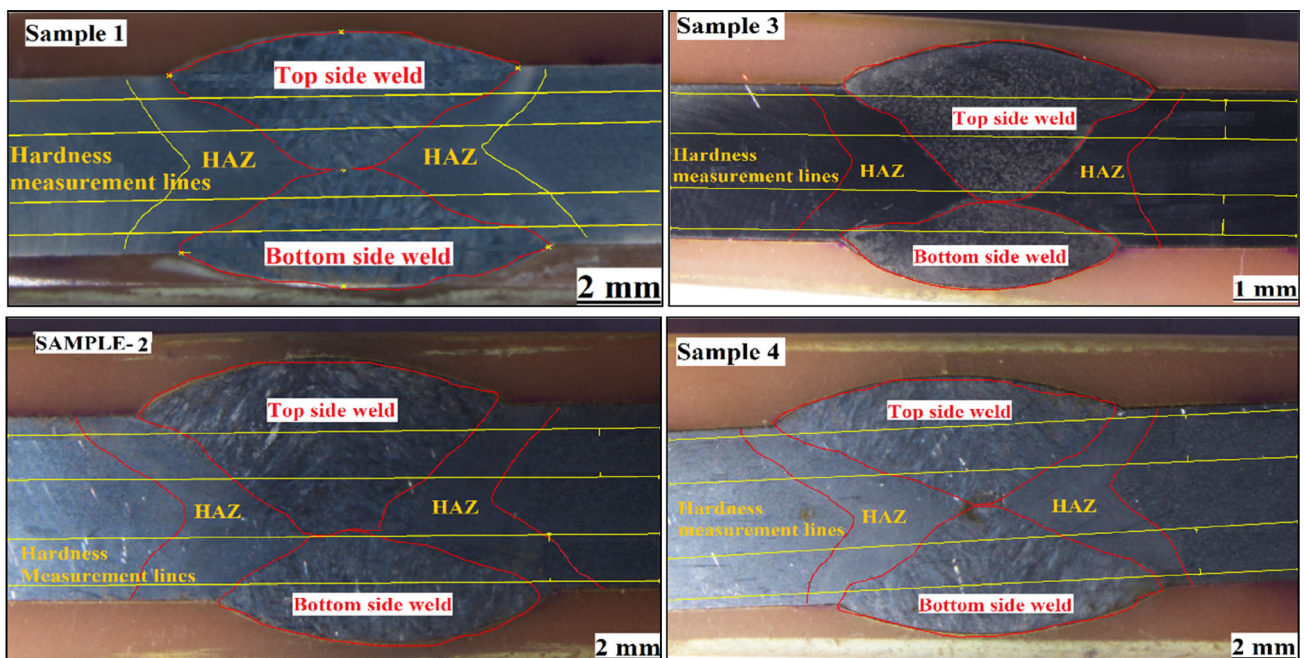


**Fig. 3** Cross-sectional view of the weld sample in four cases

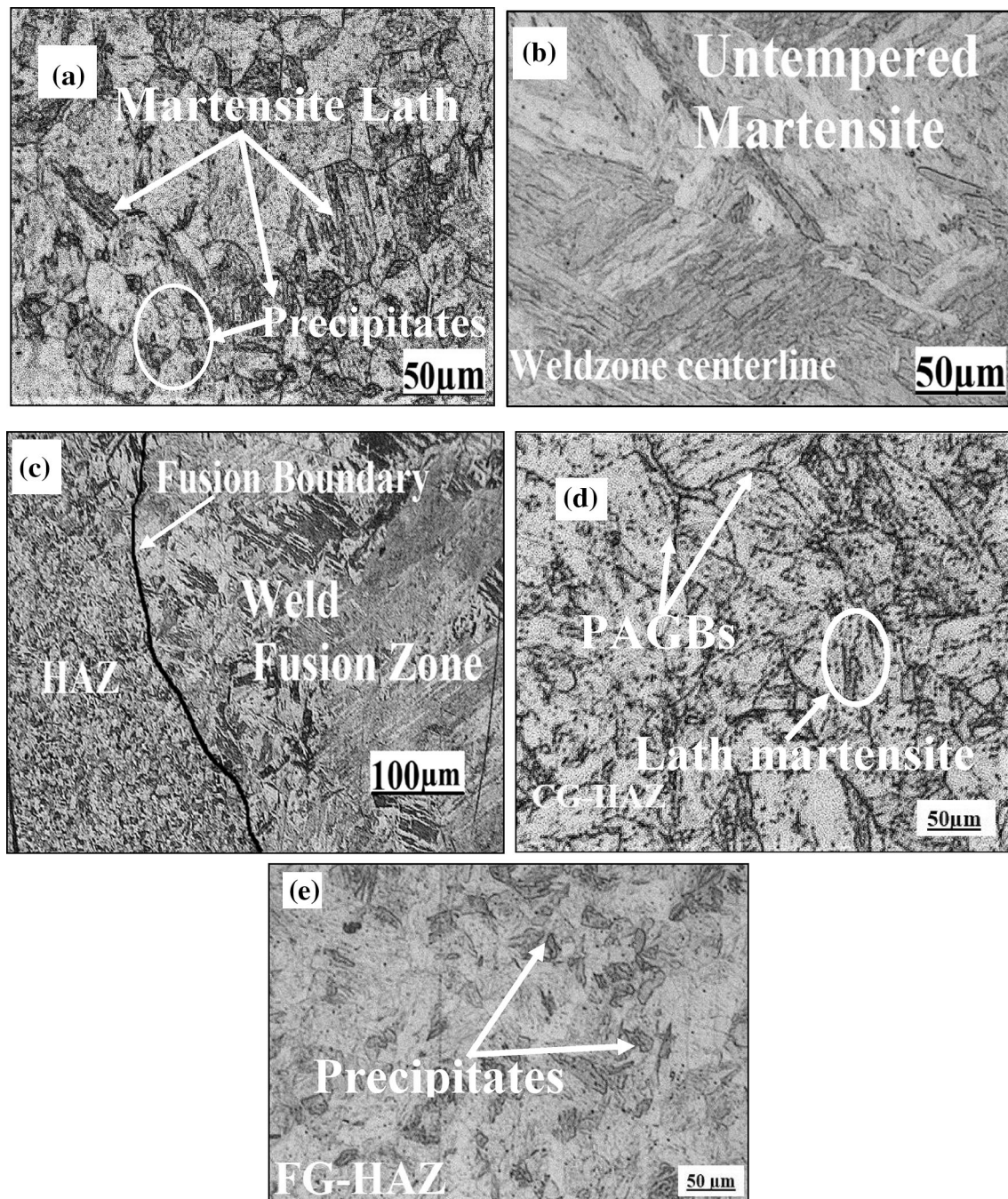


**Fig. 4** Microstructure images of as-welded weld: **a** base metal, **b** centreline of weld zone, **c** fusion boundary line with fusion zone and HAZ, **d** CG-HAZ, **e** FG-HAZ

### 3 Results and Discussion

#### 3.1 Macro- and Micrographical Study

The properly etched samples were captured on the digital camera. Macrographs for all the four samples are shown in Fig. 3. It is observed that with SAW process, the weld penetration is obtained about 50% of the weld thickness in

a single pass. However, for preheated samples, i.e. Samples 2 and 3, it increases up to 60–70% of the plate thickness. The fusion boundary and HAZ boundary are also presented in Fig. 3. It also shows the hardness lines along the transverse direction of the weld zone over which hardness is measured.

The HAZ regions are observed to be about 20% of the weld bead width. The microstructure is observed for all the

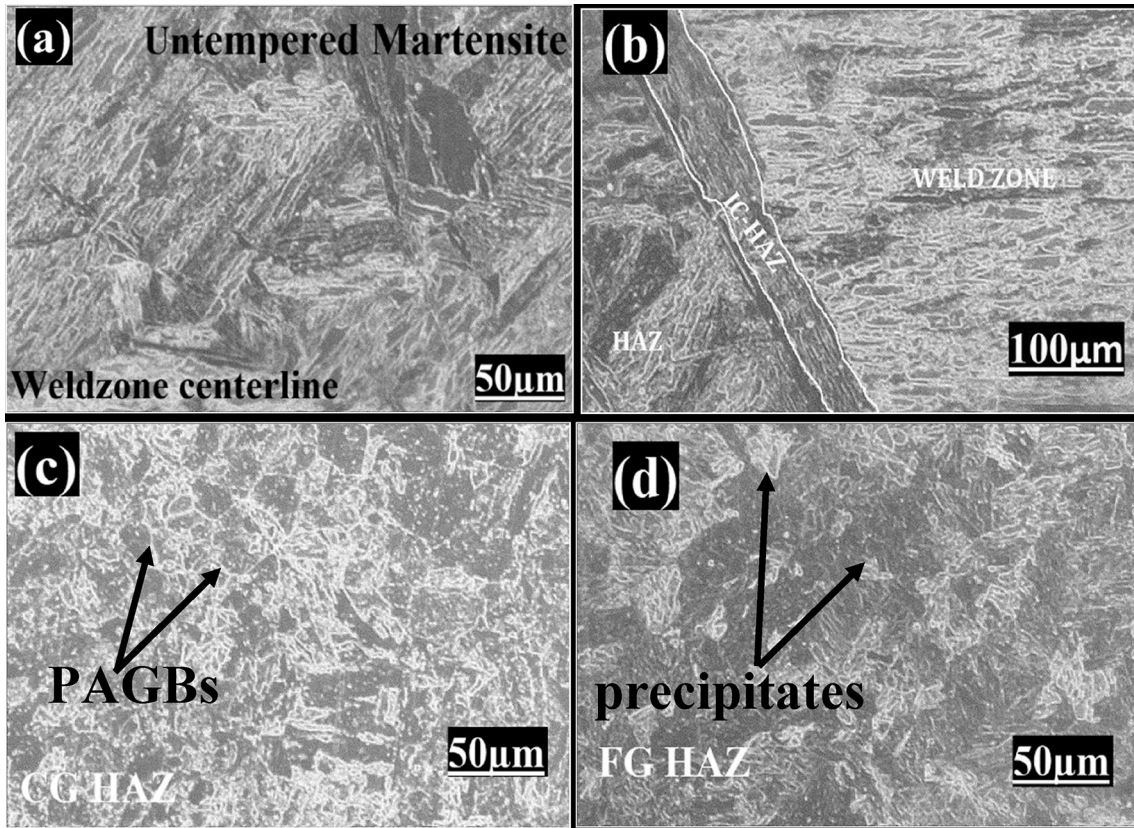


**Fig. 5** Microstructure images of preheated weld: **a** weld zone centreline, **b** fusion boundary line with fusion zone and HAZ, **c** CG-HAZ, **d** FG-HAZ

**Fig. 6** Microstructure images of PWHT weld: **a** weld zone centreline, **b** fusion boundary line with fusion zone and HAZ, **c** CG-HAZ, **d** FG-HAZ

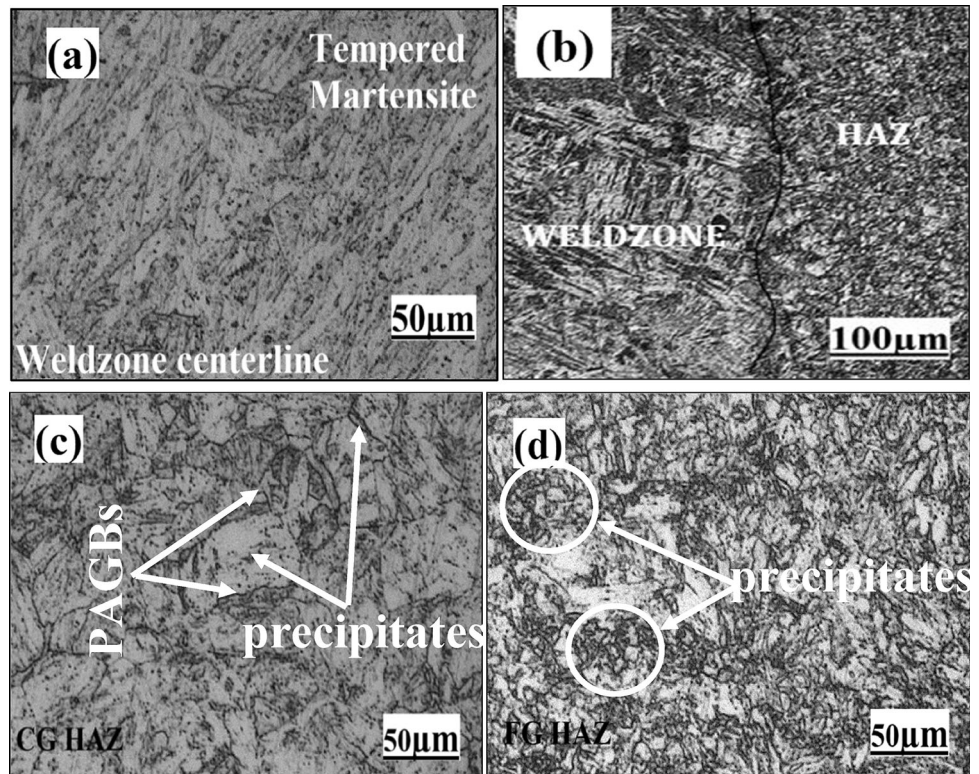
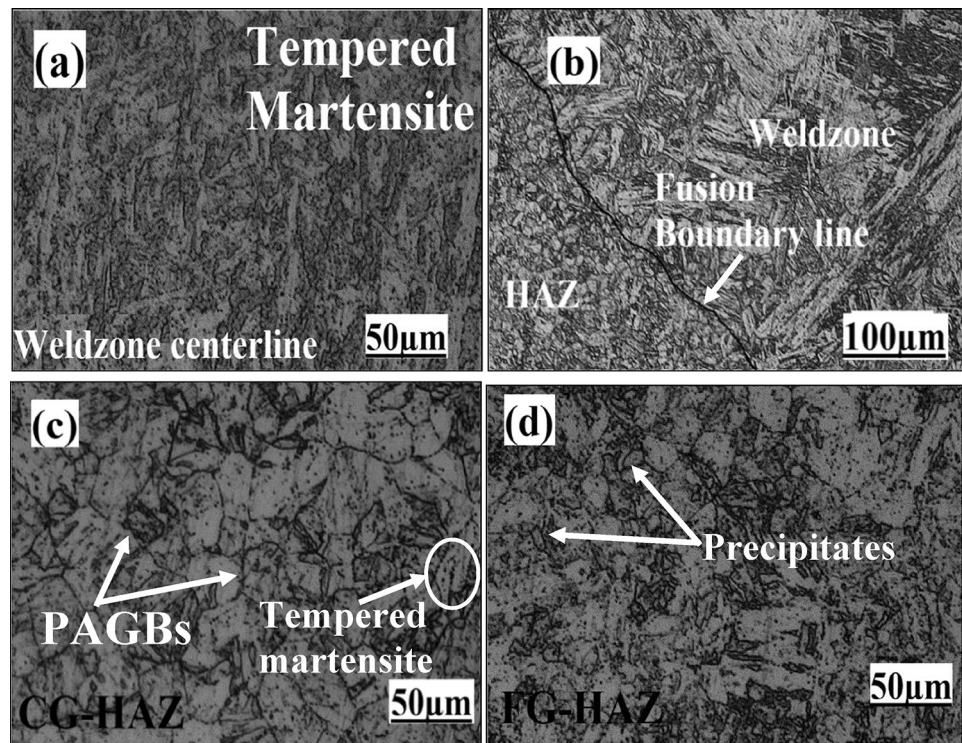


**Fig. 7** Microstructure images of preheated and PWHT weld: **a** weld zone centreline, **b** fusion boundary line with fusion zone and HAZ, **c** CG-HAZ, **d** FG-HAZ



four cases in different weld zones, i.e. FZ, CG-HAZ, FG-HAZ, IC-HAZ separately. Figure 4 reveals the microstructure of the as-welded sample for different regions across the weld. The martensitic lath structure in between the polygonal ferrite and pearlite grains structure is observed in P91 steel base plate. The presence of carbide precipitates like  $M_{23}C_6$  and MX also characterises the P91 steel microstructure.

Figure 4b exhibits the needle-shaped or acicular untempered martensite structure in fusion zone. The high thermal gradient in the weld centreline promotes comparatively higher cooling rate and so transforms into martensite structure during solidification. Figure 4c shows the fusion boundary line between fusion zone and HAZ. The coarse-grained HAZ adjacent to FZ is observed within  $\sim 3.5$  mm of width. Figure 3d comprises of coarse austenitic grains boundary owing to moderate thermal gradient in the region. The untempered martensite lath is clearly observed within the PAGBs indicated by arrows. For moderate peak temperature (above transformation temperature ( $A_{c3}$ )), precipitates get dissolved to form carbide and nitride matrix which results in lath martensite in CG-HAZ.

The FG-HAZ is also shown in Fig. 4e in the width of  $\sim 1.5$  mm. The peak temperature in FG-HAZ remains below the transformation temperature ( $A_{c3}$ ) and so, the precipitates present can not completely dissolve, which is easily observed in Fig. 4e [9, 25]. Hence, the whole width of HAZ is observed with in the width of  $\sim 5$  mm near the

region half of the thickness of the plate. Figure 5 presents the microstructural images of preheated weld sample. In fusion zone, untempered martensite (needle-shaped) grains are observed similar to as-welded case as shown in Fig. 5a. Nonetheless, as the preheating process decreases the thermal gradient from fusion zone towards HAZ, it diminishes the formation of columnar structure during solidification. In CG-HAZ, the austenitic grain size is observed to be smaller than the as-welded sample owing to high heating rate as a result of preheating near the root gap [21]. The microstructures of different zones for post-weld heat-treated weld are shown in Fig. 6. Coarsening of carbide precipitates are clearly observed after PWHT. The austenitic grain size collectively increases in CG-HAZ and FG-HAZ as observed in Fig. 6c, d. On PWHT, tempering process take place which converts the needle-shaped martensitic structure to fine-grained ferritic matrix embedded with cementite particles which are clearly observed as black spots in the microstructure as shown in Fig. 6a. Both coarse-grained HAZ and fine-grained HAZ show the tempered martensite along with coarse and fine prior austenitic grains. Figure 7 presents the micrographs of preheated and PWHT weld joint for various zones across the weld [7]. As PWHT was carried out on a preheated weld joint, the effect of preheating is not noticeable from the microstructural images. However, in weld zone region, the tempered martensite consists of both ferrite and pearlite grain matrix along with cementite particles.

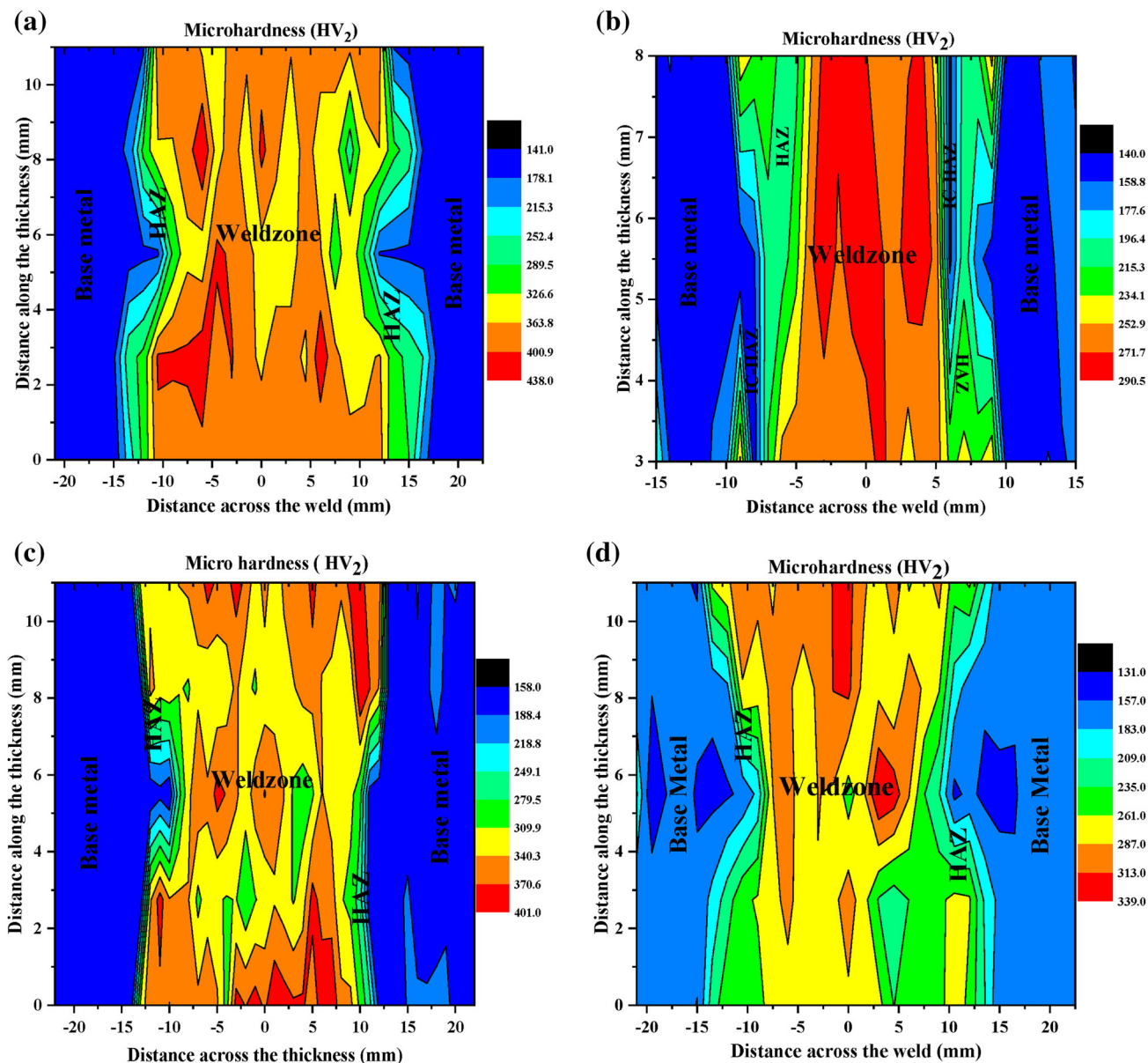


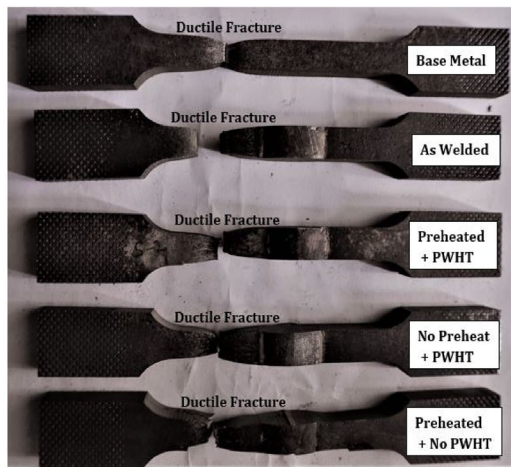
**Fig. 8** Contour plot of hardness values for **a** as-welded weld, **b** preheated and PWHT weld, **c** preheated weld, **d** post-weld heat-treated weld

### 3.2 Microhardness of Welds

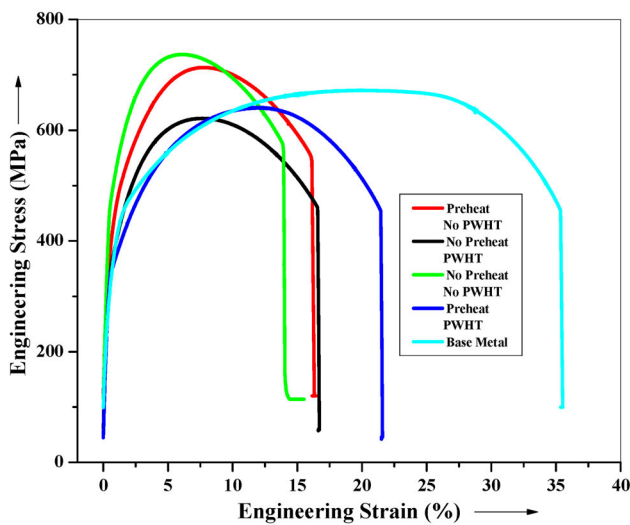
The contour plots of microhardness values of the four welding samples are shown in Fig. 8a–d. From the contour plot, it is observed that the hardness values vary for different zones of weldments and base metal. For ‘Sample 1’, the hardness distribution observed in FZ is comparatively higher with the maximum hardness value of 438HV. On performing PWHT, the hardness value reduces to much lower values owing to complete tempering of martensite which results in softening of the material. It can be observed in both the cases of ‘Sample 2’ and ‘Sample 4’ that the average hardness values in the FZ reduce to 165HV and 178HV, respectively. Similarly, the minimum hardness

value in the weld zone is observed for Sample 2 as 174HV. It is observed that preheating individually reduces the hardness value from 437.2 HV (Sample 1) to 401 HV (Sample 3), i.e. by 8.2%. Similarly, the combined preheating and PWHT reduce the hardness value from 437.2 HV (Sample 1) to 174 HV (Sample 2), i.e. by 60.2%. It is noticeable that in Samples 1 and 3, the hardness values suddenly drops at the boundary of FZ and HAZ, which designates the presence of intercritical HAZ. This sudden fall in hardness value makes the Gr. 91 welds prone to cracking and failure. On the other hand, due to the application of preheating and PWHT, the hardness values reduce to much lower values. From Fig. 8a, it is clearly observed that for as-welded condition, the hardness values





(a)



(b)

**Fig. 9** a Test specimens after ductile fracture, b engineering stress versus engineering strain curve at room temperature

have different peak values for fusion zone, whereas, on preheating, the austenitic grain size in HAZ reduces and grains become less columnar in fusion zone. This decreases the overall hardness values in both HAZ and FZ with more

smooth and uniform distribution across the fusion zone which is also clearly visible in Fig. 8b. On the basis of observation and studies on microhardness and correlating microstructural changes, it can be said that grain structure, size, grain boundaries and matrix get affected and phase changes during heat treatment affect the microhardness values. The microhardness test is also performed along the weld joint in the fusion zone. From the results it is observed that the microhardness values remain unchanged throughout the weld length as it possesses the same microstructural condition.

### 3.3 Weld Strength and Ductility

To evaluate the actual weld strength of the welds, the tensile specimens have been prepared along with the weld bead. It examines the quality of the weld bead for any welding defects. Fracture location has been verified which must be away from the weld fusion zone. Two tensile samples are prepared for each welding cases. The average values of the two for each case have been reported as the final results. The tensile samples after conducting the test are also displayed in Fig. 9a which exhibits the fracture region which is within the base plate far away from the weld region for all the cases. The engineering stress versus strain plot is obtained for each tensile test conducted at the room temperature which is collectively shown in Fig. 9b. The nature of the fracture is ductile for each case which differs with the degree of ductility. To ensure the nature of the fracture, fractography has also been conducted. Hence, the Sample 1 and Sample 3 show the higher UTS of 740 MPa and 721 MPa, respectively. With PWHT process, UTS reduces to 618 MPa and 627 MPa for Sample 2 and Sample 4, respectively. On performing PWHT, the martensite gets tempered to reduce the hardness value, resulting in lower ultimate tensile strength and more ductility of the weld. It also causes softening of the welds with the reduced hardness values.

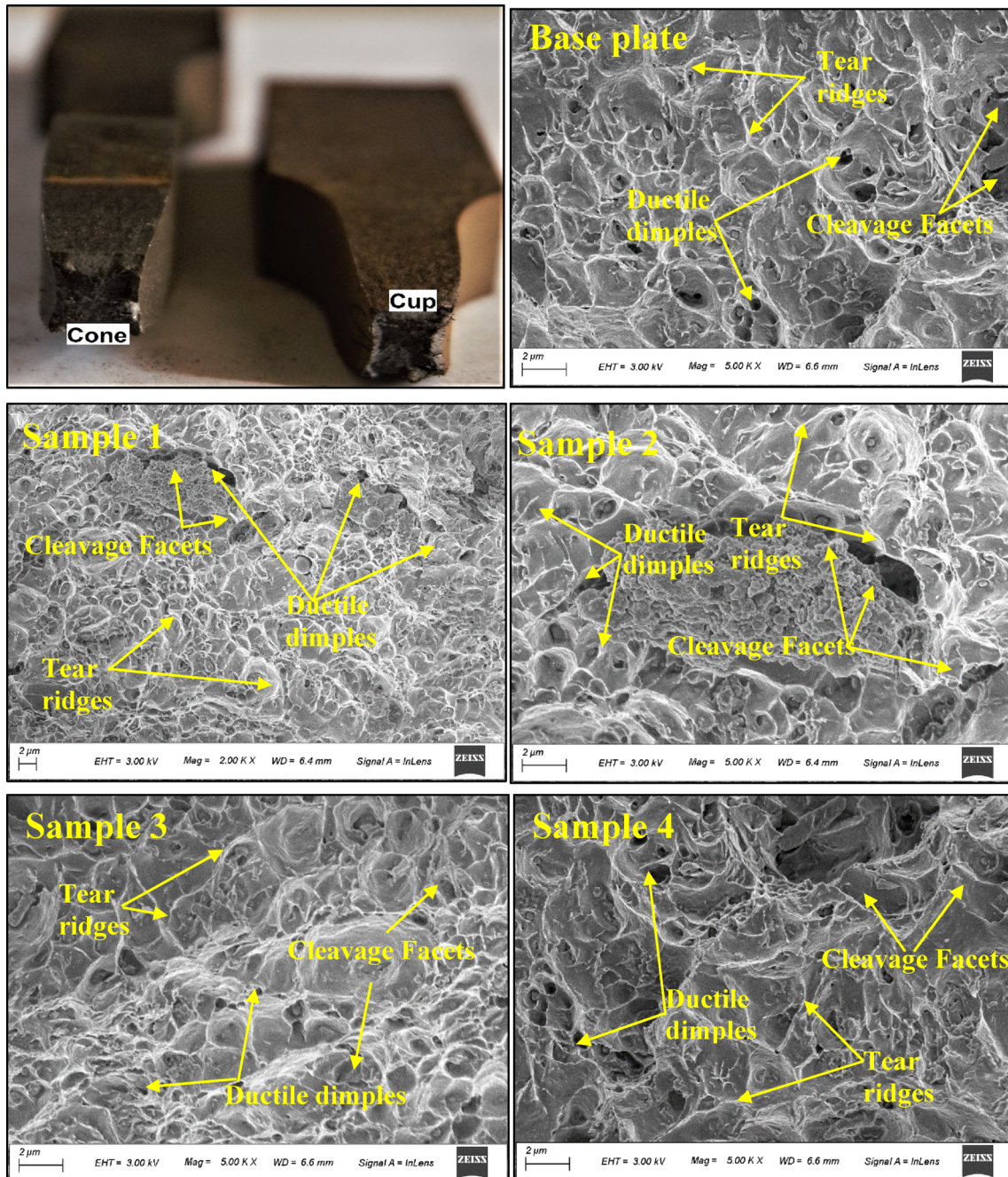
Table 4 presents the UTS, YS and % elongation values for all five tensile test cases. The table also includes the break point strength values. However, both the individual

**Table 4** Tensile test results for four cases and P91 steel plate

Sl. no.	Sample	Ultimate tensile strength (MPa)	0.2% offset yield strength (MPa)	Strength at fracture (MPa)	% Elongation	Fracture location
1.	As-welded	740	513	564	14.6	Base plate
2.	Preheat + PWHT	618	389	409	22.2	Base plate
3.	Preheat + no PWHT	721	488	554	16.2	Base plate
4.	No preheat + PWHT	627	396	473	18.6	Base plate
5.	Base metal	651	437	421	35.6	Base plate

**Table 5** Variation (%) in UTS, YS and ductility of welded joint due to preheating and PWHT processes

Sl. no.	Processes	Ultimate tensile strength (% decrement)	Yield strength (% decrement)	Ductility (% increment)
1.	Preheating	2.6	4.9	11
2.	PWHT	15.2	22.8	27.4
3.	Preheating + PWHT	16.5	24.2	52

**Fig. 10** Necking area and scanned electron micrograph of fractured surfaces of the tensile specimens of all different cases, fractured under the tensile test conducted at room temperature

and combined processes improve the ductility of the welded joints. The percentage variations of UTS, YS and ductility are also presented in Table 5. It is observed that preheating alone improves the ductility of the welded joint by 11%. PWHT improves the ductility of the weld by 27.4%. And if PWHT is performed on preheated sample, ductility increases by 52%. However, for the same case, the weld strength, i.e. UTS and YS, reduce by 16.5% and 24.2%, respectively. Similar reduction is observed in other welding processed P91 steel joints [22, 23]. Hence, the Sample 1 and Sample 3 show the higher UTS of 740 MPa and 721 MPa, respectively. With PWHT process, UTS reduces to 618 MPa and 627 MPa for Sample 2 and Sample 4, respectively. On performing PWHT, the martensite gets tempered to reduce the hardness value, resulting in lower ultimate tensile strength and more ductility of the weld. It also causes softening of the welds with the reduced hardness values.

The microstructural evolutions and variations in mechanical properties owing to pre- and post-welding processes indicate a great interrelationship between them. On preheating, the cooling rate gets slowed down, which results in an increase in the fraction of the dark surrounding ferrite phase with coarsened dendrite structure causing better ductility of the weld. It also decreases the austenitic grains size which decreases the hardness values as well as the YS and UTS. Similarly, post-weld heat-treated weld or say weld after tempering converts the acicular martensite structure to fine-grained ferrite structure which softens the matrix and reduces the resistance against plastic deformation. It results in deduction in hardness and improvement in ductility. The coarsening of cementite particles and equiaxed ferrite grains reduces the dislocation density in the post-weld heat-treated welds which also contributes to reduction in the YS and UTS values. The joint efficiency of as-welded sample is observed to be 114%, which reduces to 110%, 97% and 95% on preheating, post-weld heat treatment and combined preheating and post-weld heat treatment, respectively [26, 27].

The necking areas as shown in Fig. 10 present the cup and cone shape of the fractured portion. Such cup and cone shape is generated from combination of the shear failure planes at 45° with the axis of the specimen at each peripheral crack surfaces towards the central axis. Therefore, such appearance assures the occurrence of ductile failure. The electron microscopic fracture surface images consist of ductile tear ridges, ductile dimples and cleavage facets, etc. The presence of equiaxed and spherical dimples and voids reveals a transgranular fracture of the specimens. The number of ductile dimples increases in the case of ‘Sample 2’ and ‘Sample 4’, i.e. after preheating process on ‘Sample 1’ and ‘Sample 3’, and hence indicates better ductility of the welded joint. Similarly, a smaller number of

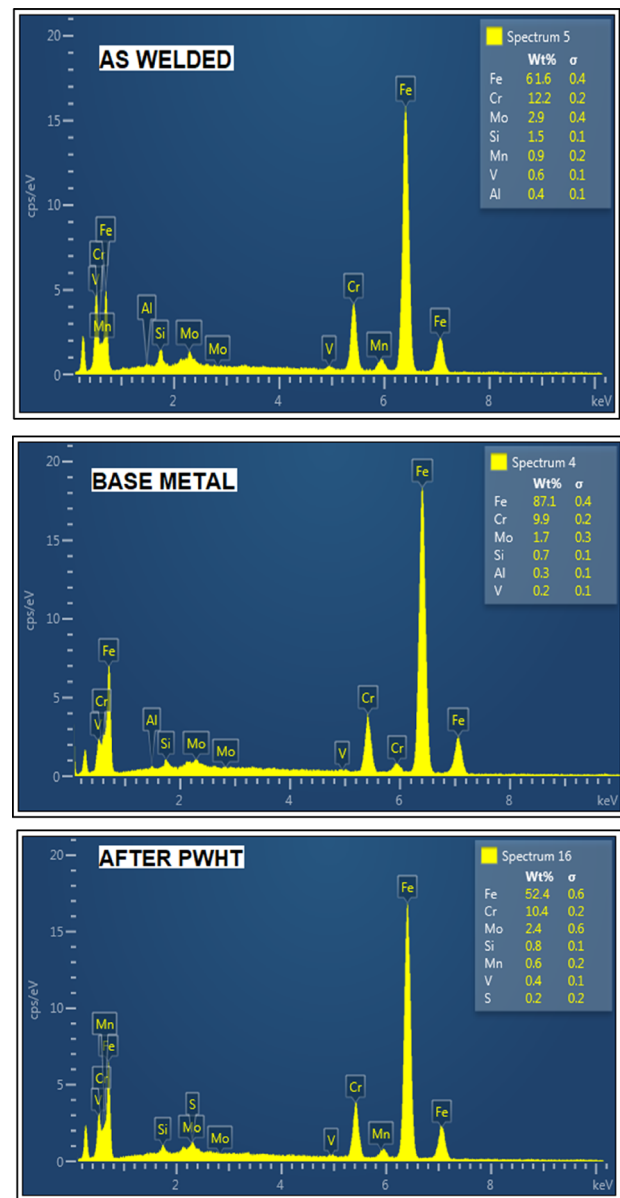


**Fig. 11** EDS of the metal surface for different conditions: **a** base metal, **b** as-welded condition, **c** weld after PWHT

cleavage facets as well as smaller cleavage facets also decrease the possibility of brittle fracture in P91 steel, i.e. a polycrystalline metal welded joint [23, 28].

The presence of different elements on the crack surfaces of different welding cases is also influenced by pre- and post-welding heat treatments. Hence, this is also analysed through energy-dispersive (X-ray) spectroscopy of top surfaces in the crack regions. The X-ray peaks of different elements present on the targeted surfaces are shown in Fig. 11, which provides the wt% of those elements directly. The major elements which are present there in all the cases are Fe, Cr, Mo, Mn, V, C, Si, Al, etc. The abundance of Mn and Mo in the as-welded weld signifies the higher weld

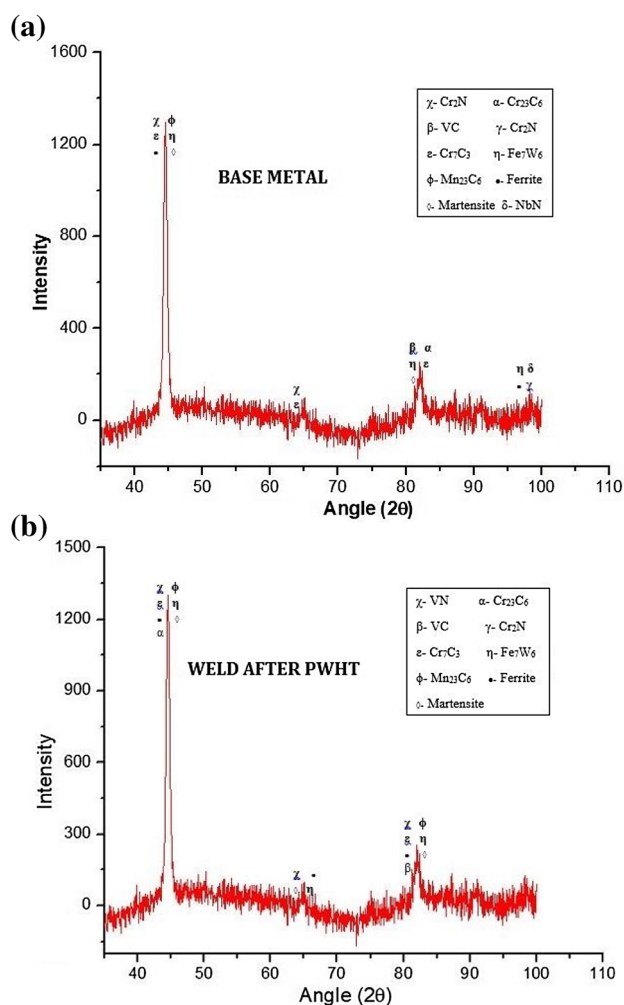


**Fig. 12** X-ray diffraction intensity plots for **a** base metal, **b** weld after PWHT

strength as compared to preheated and post-weld heat-treated welds [2]. Similarly, the presence of carbide- and nitride-forming elements Cr and V develops precipitates like  $\text{Cr}_{23}\text{C}_6$ , VN, VC, etc., which improves the creep strength of the weld after PWHT. The existence of such precipitates is also verified with X-ray diffraction results comparing base metal and post-weld heat-treated metal as shown in Fig. 12. The different phases indicate the presence of different precipitates like VC,  $\text{Cr}_7\text{C}_3$ ,  $\text{Mn}_{23}\text{C}_6$ , and  $\text{Cr}_{23}\text{C}_6$ ,  $\text{Cr}_2\text{N}$ , NbN,  $\text{Fe}_7\text{W}_6$ , etc. The presence of similar phases has also been reported by other researchers as well [9, 23, 29].

## 4 Conclusion

A study was executed to examine the effect of preheating and PWHT processes on the submerged-arc-welded double-sided square butt joint of P91 steel. The study included

microstructural and mechanical properties characterisations, fractography, EDS and XRD analyses of the welds. Based on the above study, the following conclusions were made:

- Preheating process can improve the depth of penetration and bead shape quality.
- It was observed that preheating softened the FZ of P91 weld joint by 8.2% and 10.4% for as-welded and post-weld heat-treated welds owing to decrease in austenitic grain size in FZ.
- Preheating also reduced the UTS and YS by 2.6% and 4.87%, respectively, from the as-welded condition because high heating rate from preheating reduced the austenitic grain size.
- It was observed that the preheating-induced slow cooling rate in preheated and combined preheated and PWHT welds increased the ductility as compared to as-welded weld.
- PWHT induced tempered martensite or say equiaxed fine-grained ferrite with cementite particles which softened the matrix and reduced the microhardness values in the FZ and HAZ of the weld similar to the as-received base metal.
- It was observed that on PWHT, the fractional area of the carbide precipitates increased which reduced the UTS and YS of post-weld heat-treated and combined preheated and post-weld heat-treated welds.

## Compliance with Ethical Standards

**Conflict of interest** The authors declare that they have no conflict of interest.

## References

1. El-azim M E A, Nasreldin A M, Zies G, and Klenk A, *Mater Sci Technol* **21** (2005) 779, <https://doi.org/10.1179/174328405x43216>.
2. Pandey C, Mohan M, Kumar P, and Saini N, *J Alloys Compd* **743** (2018) 332, <https://doi.org/10.1016/j.jallcom.2018.01.120>.
3. Pandey C, Giri A, and Mahapatra M M, *Mater Sci Eng A* **664** (2016) 58, <https://doi.org/10.1016/j.msea.2016.03.132>.
4. Francis J A, Mazur W, and Bhadeshia H K D H, *Review Type IV Cracking in Ferritic Power Plant Steels, Type IV Cracking in Ferritic Power Plant Steels*, vol. 0836 (2013), <https://doi.org/10.1179/174328406x148778>.
5. Cohn M J and Henry J F, *Fabrication, Construction, and Operation Problems for Grade 91 Fossil Power Components* (2016), <https://doi.org/10.1115/1.1904054>.
6. Coleman K and Newell W, *Weld J-NY*, **86** (2007) 29.
7. Pandey C and Mahapatra M M, *J Mater Eng Perform* **25** (2016) 2195, <https://doi.org/10.1007/s11665-016-2064-x>.
8. Mahapatra C P M M, *Trans Indian Inst Met* **69** (2016) 1657, <https://doi.org/10.1007/s12666-015-0826-z>.
9. Pandey C, Giri A, and Mahapatra M M, *Mater Sci Eng A* **657** (2016) 173, <https://doi.org/10.1016/j.msea.2016.01.066>.

10. Weman K, in *Welding Process Handbook*, 2nd edn., Sicensidirect (2012), p. 105.
11. Santella M L, Swindeman R W, Reed R W, and Tanzosh J M, *Martensite Formation in 9 Cr-1 Mo Steel Weld Metal and Its Effect on Creep Behavior*.
12. Zhang S, Melfi T, and Narayanan B K, *Sci Technol Weld Join*, **21** (2016) 147.
13. Roy J, Rai R N, and Saha S C, *Evaluation of Microstructure and Mechanical Properties of P91 Steel Weldment Due to Addition of Boron Trioxide into Flux During Submerged Arc Welding* (2017), <https://doi.org/10.1007/s40194-017-0515-0>.
14. Rao R V and Kalyankar V D, *Int J Adv Manuf Technol* **69** (2013) 93, <https://doi.org/10.1007/s00170-013-5007-9>.
15. Suman S, Biswas P, Kumar S, Pratap V, Kumar A, and Kuriachen B, *Mater Today Proc* (2019). <https://doi.org/10.1016/j.matpr.2019.12.049>.
16. Suman S and Biswas P, *J Manuf Process* **51** (2020) 19, <https://doi.org/10.1016/j.jmapro.2020.01.012>.
17. Suman S and Biswas P, *Mater Today Proc* (2020). <https://doi.org/10.1016/j.matpr.2019.12.299>.
18. Suman S and Biswas P, *Advances in Mechanical Engineering. Lecture Notes in Mechanical Engineering*, Springer, Singapore (2020).
19. Suman S, Pankaj P, Tiwari A, Biswas P, Kuriachen B and Sinha A, *Advances in Additive Manufacturing and Joining. Lecture Notes on Multidisciplinary Industrial Engineering*, Springer, Singapore (2020).
20. Singh A K, Dey V, and Rai R N, *J Manuf Process*, **25** (2017) 1, <https://doi.org/10.1016/j.jmapro.2016.09.006>.
21. Sireesha M, Sundaresan S, and Albert S, *J Mater Eng Perform* **10** (2001) 320, <https://doi.org/10.1361/105994901770345033>.
22. Dhandha K H and Badheka V J, *J Manuf Process* **17** (2015) 48, <https://doi.org/10.1016/j.jmapro.2014.10.004>.
23. Pandey C, Mahapatra M M, Kumar P, and Kumar S, *J Mater Process Tech* **266** (2018) 140, <https://doi.org/10.1016/j.jmatprotec.2018.10.024>.
24. Pandey C and Mahapatra M M, *J Mater Eng Perform* **25** (2016) 2761, <https://doi.org/10.1007/s11665-016-2127-z>.
25. Pandey C, Giri A, Mahapatra M M, and Kumar P, *Met Mater Int* **23** (2017) 12, <https://doi.org/10.1007/s12540-017-6394-5>.
26. Gopal J, Pandey C, Mohan M, and Mulik R S, *J Manuf Process* **48** (2019) 249, <https://doi.org/10.1016/j.jmapro.2019.10.002>.
27. Chaurasia P K, Pandey C, Giri A, Saini N, and Mahapatra M M, *Arch Metall Mater* **63** (2018) 1019, <https://doi.org/10.24425/122437>.
28. Pandey C, Saini N, Mahapatra M M, and Kumar P, *Eng Fail Anal* **71** (2016) 131, <https://doi.org/10.1016/j.engfailanal.2016.06.012>.
29. Hurtado-noreña C, Danón C A, Luppo M I, and Bruzzoni P, *Proc Mater Sci* **8** (2015) 1089, <https://doi.org/10.1016/j.mspro.2015.04.172>.

**Publisher's Note** Springer Nature remains neutral with regard to jurisdictional claims in published maps and institutional affiliations.